| | |
|---|---|
| ***Publication Year*** | 2018 |
| ***Acceptance in OA*** | 2021-02-26T16:29:54Z |
| ***Title*** | Investigating Sources of Mercury's Crustal Magnetic Field: Further Mapping of MESSENGER Magnetometer Data |
| ***Authors*** | Hood, Lon L., Oliveira, Joana S., GALLUZZI, VALENTINA, Rothery, David Alan |
| ***Publisher's version (DOI)*** | 10.1029/2018JE005683 |
| ***Handle*** | http://hdl.handle.net/20.500.12386/30654 |
| ***Journal*** | JOURNAL OF GEOPHYSICAL RESEARCH (PLANETS) |
| ***Volume*** | 123 |

AGU100 ADVANCING EARTH AND SPACE SCIENCE

JGR

Journal of Geophysical Research: Planets

**RESEARCH ARTICLE**

10.1029/2018JE005683

**Key Points:**

- Crustal magnetic anomalies correlate with some impact basins/craters on Mercury but not others
- A possible explanation is that some impactors added more ferromagnetic material to the interiors and ejecta of the craters they produced
- The metallic iron added by impactors is unlikely to explain the observed anomalies as being induced rather than remanent

**Supporting Information:**

- Table S1

**Correspondence to:**
L. L. Hood,
lon@lpl.arizona.edu

**Citation:**
Hood, L. L., Oliveira, J. S., Galluzzi, V., & Rothery, D. A. (2018). Investigating sources of Mercury's crustal magnetic field: Further mapping of MESSENGER magnetometer data. *Journal of Geophysical Research: Planets*, *123*. https://doi.org/10.1029/2018JE005683

Received 14 MAY 2018
Accepted 24 AUG 2018
Accepted article online 29 AUG 2018

# Investigating Sources of Mercury's Crustal Magnetic Field: Further Mapping of MESSENGER Magnetometer Data

**L. L. Hood**[1], **J. S. Oliveira**[2,3], **V. Galluzzi**[4], **and D. A. Rothery**[5]

[1]Lunar and Planetary Laboratory, University of Arizona, Tucson, AZ, USA, [2]ESA/ESTEC, SCI-S, Noordwijk, Netherlands, [3]CITEUC, Geophysical & Astronomical Observatory, University of Coimbra, Coimbra, Portugal, [4]Instituto di Astrofisica e Planetologia Spaziali, INAF, Rome, Italy, [5]School of Physical Sciences, Open University, Milton Keynes, UK

**Abstract** One hundred six low-altitude passes of magnetometer data from the last 2 months of the MErcury Surface, Space ENvironment, GEochemistry, and Ranging mission have been applied to produce a map of the crustal magnetic field at a constant altitude of 40 km covering latitudes of 35–75° N and longitudes of 270–90° E. Some anomalies correlate significantly with impact basins/craters (e.g., Rustaveli and Vyasa), while other basins/craters have no obvious anomalies. A possible interpretation that is consistent with lunar evidence is that some impactors delivered more ferromagnetic Fe–Ni metal to the interior subsurfaces and ejecta fields of the craters/basins that they produced. The amount of metallic iron that could plausibly be delivered is limited by the diameter and mass of an impactor that would yield a crater with observed diameters (e.g., 200 km for Rustaveli). This in turn limits the maximum amplitude of anomalies that could be induced by impactor-added iron in the present-day Mercury global field to relatively low values. It is therefore concluded that if impactor-added iron is the source of the observed crater-associated anomalies, then they must be almost entirely a consequence of ancient remanent magnetization. A broad magnetic anomaly occurs over the northern rise, a topographically high region with an associated strong free air gravity anomaly. A possible interpretation of the latter anomaly is that an early major impact preconditioned the region for a later mantle uplift event.

**Plain Language Summary** The origin of crustal magnetic anomalies on heavily cratered, airless bodies like the Moon and Mercury remains uncertain. Mapping of MErcury Surface, Space ENvironment, GEochemistry, and Ranging magnetometer data at northern midlatitudes on Mercury shows that magnetic anomalies are concentrated near and within some impact basins and craters but not others. The association of anomalies with some craters but not others is consistent with the hypothesis that metallic iron in some impactors (either in an iron core or distributed in the body) was mixed into impact melt and ejecta which then became magnetized while cooling in a former core dynamo magnetic field. Other impactors containing little metallic iron (e.g., cometary nuclei) would have produced no magnetic anomalies. The amount of metallic iron that could plausibly have been delivered by impactors is too small to explain observed anomaly amplitudes as being induced by permeability in the present-day Mercury global magnetic field. Permanent (*remanent*) magnetization originating in the early history of the planet is therefore required. One magnetic anomaly is found over the northern rise, a topographically high region with a strong gravity anomaly. This anomaly may indicate that an early major impact weakened the outer lithosphere, allowing a later mantle plume to uplift the region.

## 1. Introduction

A valuable data set for investigating crustal magnetism on Mercury was obtained by the NASA MErcury Surface, Space ENvironment, GEochemistry, and Ranging (MESSENGER) Discovery mission during the final year of its existence (Johnson et al., 2015). Altitude-normalized maps of the crustal field covering part of one side of the planet (mainly 90° E to 270° E and 35° N to 75° N) have previously been constructed from low-altitude magnetometer data using an equivalent source dipole (ESD) technique (Hood, 2015, 2016; hereafter H15 and H16). Results showed that the strongest crustal field anomalies in this region are concentrated around and within the 1,550-km-diameter Caloris impact basin. A second smaller concentration was mapped over and around Sobkou Planitia, which contains a much older 770-km-diameter impact basin. In general, anomalies over high-reflectance volcanic plains were relatively weak, while anomalies over low-reflectance material that has been reworked by impact processes were relatively strong. Overall, these results suggested that at least some of Mercury's crustal sources consist of impact melt rocks within impact basins and in externally deposited ejecta, as has also been inferred from lunar studies (Halekas et al., 2001; Hood, 2011; Hood et al., 1979, 2013; Strangway et al., 1973; Wieczorek et al., 2012). Because of the long cooling time following a basin-forming impact, the strong anomalies within the Caloris rim were interpreted as implying the existence of a steady core dynamo at the time when this basin formed (3.8 – 3.9 Gyr ago assuming an age comparable to that of the youngest lunar impact basins).

In this work, results of mapping low-altitude MESSENGER magnetometer data over part of the other side of the planet (270° E to 90° E and 35° N to 75° N) are reported. We also investigate in more detail the occurrence of anomalies associated with impact basins/craters and identify anomalies that are most probably thermoremanent in origin, that is, that may contain information about an ancient dynamo. Because Mercury presently possesses a global internal dynamo field, the possibility that some anomalies may dominantly reflect induced magnetization of permeability enhancements in the crust rather than ancient remanent magnetization is also considered.

## 2. Mapping Methods

As discussed in H15 and H16, a challenge in producing a reliable crustal magnetic field map from MESSENGER magnetometer data is the strong variation with altitude of the effective surface of observation. The latter is a consequence of the eccentric spacecraft orbit combined with the occurrence of numerous correction burns intended to delay the end of the mission. One approach toward producing a map at a constant altitude is the ESD technique (Mayhew, 1979; von Frese et al., 1981). Here we apply essentially the same "classical" ESD mapping techniques employed by H16 in order to allow direct comparisons with previous work for the 90° E to 270° E longitude range.

Figure 1a plots the surface tracks of 106 orbits of MESSENGER-calibrated magnetometer data from a period beginning on 21 March and ending on 22 April of 2015 that are selected for mapping within the region extending from 270° E to 90° E and from 35° N to 75° N. Prior to selecting these data, all other low-altitude data from the period beginning in August 2014 were carefully examined. In most cases, either the periapsis altitude of the spacecraft was higher or short-wavelength external field contributions (as judged by lack of repetition of anomalies on successive orbits) were more numerous during the earlier intervals than during the March – April 2015 period. Therefore, in order to produce a map of optimal accuracy over this region, only the March – April 2015 data are considered here.

Figure 1b plots the spacecraft altitude in kilometers along the selected orbit passes. Minimum altitudes from $<10$ up to $\sim 30$ km were reached at 55° N to 60° N with step changes occurring on 2, 6, 8, and 14 April. Altitudes as high as 60 – 70 km were reached along the northern boundary at 75° N and as high as 90 – 110 km along the southern boundary at 35° N. There is a possibility of extending the map to 80° N if altitudes up to $\sim 100$ km are allowed. However, to be consistent with the mapping of H16, only latitudes up to 75° N are mapped here.

Figure 1c plots the radial component of the measured crustal field at the spacecraft altitude, that is, before applying the ESD altitude normalization technique. Only the radial field component is considered because it is usually less affected by external field variations and the ESD technique only requires one of the three vector field components (e.g., Parker, 1991). As discussed by H16, in order to produce this map, a series of steps must be taken to (a) minimize long-wavelength fields of noncrustal origin, (b) edit and interpolate the residual fields to minimize short-wavelength variations that do not repeat on successive orbit passes, and (c) two-dimensionally filter the remaining data after sorting and averaging in 0.5° latitude by 1.0° longitude bins. The specific methods adopted for carrying out these steps have been previously described in detail by H16. Also, a series of figures in the supporting information of H16 illustrate the application of those methods.

Briefly, noncrustal fields (including both magnetospheric fields and the global planetary field) were minimized in four substeps. First, to reduce long-wavelength fields, a cubic polynomial was least squares fitted to the raw radial component time series for each orbit pass. An alternate approach of removing a recent model for the global planetary field (based on the approach of Oliveira et al., 2015) prior to high-pass filtering was tried but was found to be no better than the cubic detrending method. Second, high-pass filtering in the time domain to eliminate wavelengths greater than about 215 km was done by calculating the deviation from 5° running averages (i.e., at a given point along the orbit, an average of each field component over a 5° latitude range

(a) ORBIT TRACKS

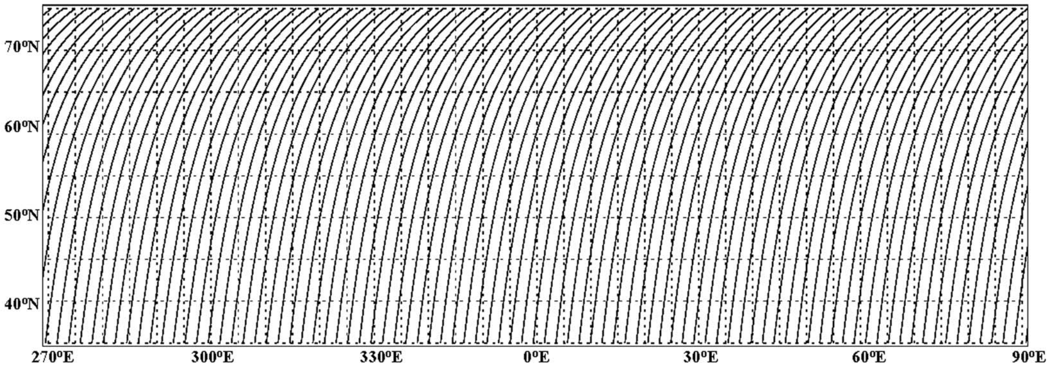

(b) SPACECRAFT ALTITUDE (km)

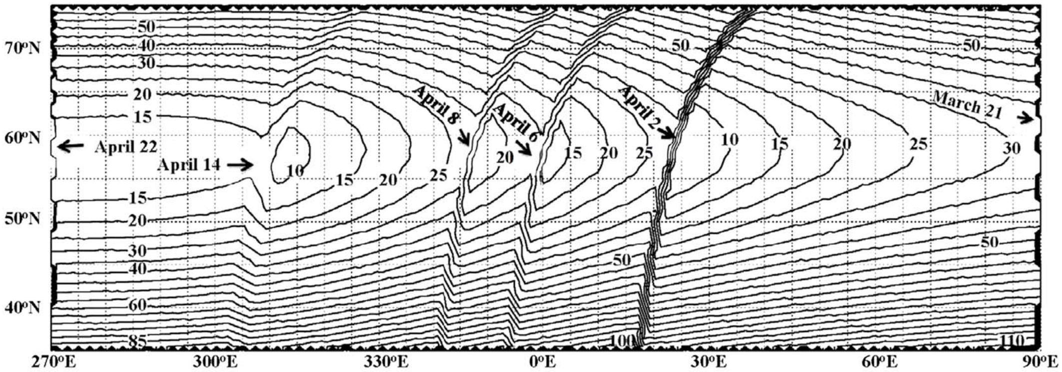

(c) B-RADIAL (nanoTeslas) at the Spacecraft Altitude

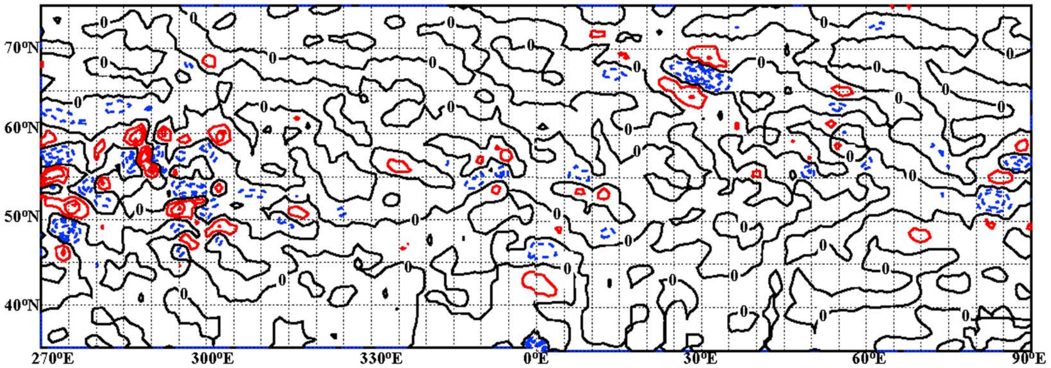

**Figure 1.** Summary of the selected MESSENGER data from March and April of 2015: (a) orbit tracks; (b) spacecraft altitude; and (c) radial magnetic field intensity at the spacecraft altitude. In (c), the contour interval is 2 nT, and negative-dashed contours are blue; positive contours are red.

centered on that point was computed and subtracted from the measured field components). Third, stack plots of the filtered radial field component for the selected orbits allowed visual identification of time intervals when excessive short-wavelength external field noise was present. See Figure S4 of H16 for examples of weak anomalies that repeat on successive orbits, verifying a crustal origin. Intervals containing field perturbations with amplitudes >1 nT that did not approximately repeat on at least one adjacent orbit were edited (deleted) from the time series. The missing data were either replaced with zero values or with values interpolated from adjacent orbits. Special care was taken to edit nonrepeating perturbations within 5° of the southern boundary at 35° N where downward continuation from the high spacecraft altitude by the ESD technique can amplify even minor external field perturbations. Of the 106 selected orbits, 47 required at least minor editing and/or linear interpolation. Nevertheless, some downward continuation errors persisted within a few degrees of the southern boundary and eastward of 10° E where the spacecraft altitude exceeded 90 km. To be conservative in preventing spurious anomalies, all measured field values at altitudes greater than 90 km were therefore set equal to 0. Fourth, two-dimensional filtering was applied after carrying out the ESD altitude correction as described in H16. One error in that description should be noted, however. It was stated that a 5 by 5 bin boxcar filter was applied after sorting and averaging the orbital measurements in 0.5° latitude by 1.0° longitude bins. In fact, a 3 by 3 boxcar filter (1.5° latitude by 3° longitude) was applied. Crustal field wavelengths shorter than about 1.5° of latitude and 3° of longitude (~64 km) and longer than about 5° of latitude (about 215 km) were therefore suppressed in both the present maps and the maps of H16.

The "classical ESD" technique that is adopted to map the radial magnetic field data of Figure 1c at a constant altitude has also been described previously in detail by H15 and H16 and is here summarized only briefly. Basically, the sources were assumed to consist of an array of vertically oriented (±90° from horizontal) magnetic dipoles separated by 1° in latitude and 2° in longitude on a spherical surface (3,731 dipoles for the longitude and latitude range considered here). A depth of 20 km below the mean planetary radius for the spherical surface was chosen to minimize the mean root-mean-square (RMS) deviation. The iterative computational method has been described in H15 with minor revisions in H16. The along-track filtered and edited data (after latitudinal binning) were fit to the dipoles; the final binning and two-dimensional filtering step was applied to the ESD model data calculated at constant altitude along the orbit tracks. To reduce computation time, the dipole array covering 190° of longitude was again divided into a series of six overlapping sectors (see Figure S2b of H16). The last 5° of the first sector and the first 5° of the second sector were discarded to avoid edge effects. This was repeated for remaining sectors. Convergence was assumed to occur when the RMS misfit decreased by less than 0.001 nT in a single iteration. This usually occurred after about 100 iterations. Final RMS deviations (misfits) in a given sector for the region considered here ranged from 0.17 to 0.43 nT (mean: 0.30 nT). This was somewhat less than the mean misfit obtained by H16 for the region on the Caloris-facing hemisphere (0.42 nT) because of the generally stronger crustal fields in that region. The overall correlation coefficient between the observed and model radial field components sampled at 0.5° resolution along the 76 orbit tracks that fall completely within the mapped area of Figure 1 was $R = 0.903$ (>5,800 data points).

## 3. Results

### 3.1. Crustal Magnetic Field

In the same format as in H16, Figure 2a shows the final model of the crustal radial field component at an altitude of 40 km, calculated using the model source dipole moments, while Figure 2b shows the field magnitude (*B-Total*). Figure 2c is a color-shaded version of Figure 2b to allow easy recognition of the strongest anomalies. A narrow zone on the southeastern border of the map is labeled "Poor Data" where observed field values were set equal to 0 to avoid downward continuation errors caused by the high spacecraft altitude. As in H16, a mapping altitude of 40 km is chosen because it is within the range of measurement altitudes and is comparable to the orbit track separation (about 50 km) at northern midlatitudes. Mapping at much lower altitudes than 40 km can lead to increased errors because the map is effectively undersampled due to the wide orbit track separation.

Comparing Figure 2a with Figure 1c, as expected, most anomalies mapped at low altitudes near the center of the latitude range are weakened, while some anomalies mapped at higher altitudes are increased in amplitude. Relatively strong anomalies are spread across an area south of 50° N, extending from about 0° E to 90° E. These anomalies merge with anomalies near 90° E mapped on the other side of Mercury (Figure 2b of H16). In addition, a number of more separated anomalies are mapped in a sector extending from 270° E to 305° E and from 35° N to 60° N. Two relatively strong (~6 nT) and fairly isolated anomalies are mapped at 275° E and 50° N and 83° E and 52° N. As discussed further below, both of the latter anomalies appear to be associated with large impact craters, while a number of other weaker anomalies may correlate with smaller craters. A relatively strong and broad anomaly is mapped near 28° E and 67° N.

### 3.2. Comparisons With Surface Geology, Topography, and Gravity

In order to investigate possible correlations between the crustal field and surface composition/geology, comparisons of the field magnitude map at 40-km altitude (Figures 2b and 2c) with a series of available maps of Mercury's surface are presented in this section. In the same format as in H16, Figure 3a is a superposition onto an enhanced color mosaic produced from MESSENGER Dual Imaging System (MDIS) data (messenger.jhuapl.edu/Explore/Images.html#global-mosaics). Figure 3b shows a superposition of the same field map onto a MESSENGER Laser Altimeter elevation map (G. Neumann, private communication, February, 2016). The contour interval in Figure 3 is reduced to 1 nT to show more details of the field distribution than can be seen in Figure 2b. Also identified in both parts of Figure 3 are major geologic features, including some named craters,

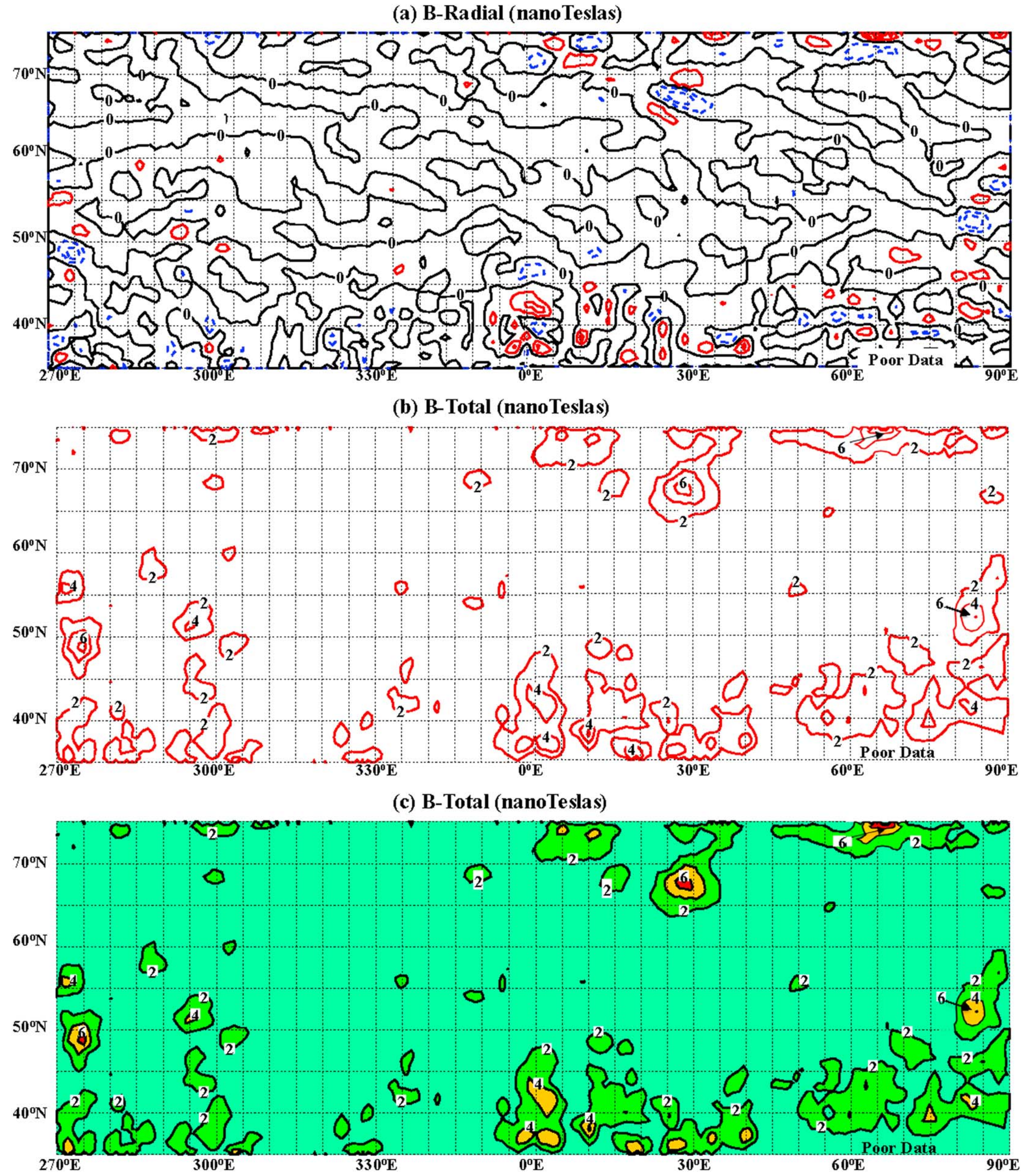

**Figure 2.** Equivalent source dipole modeling results: (a) radial magnetic field component at 40-km altitude calculated from the equivalent source dipole solution; (b) magnetic field magnitude at 40 km (contour interval, 2 nT); (c) as in (b) but shaded to emphasize stronger anomalies. The contour interval and color scheme for the radial field map are the same as in Figure 1.

certain or probable impact basins (Fassett et al., 2012), as well as a topographic high within the northern lowlands, termed the *northern rise* (Smith et al., 2012; Zuber et al., 2012).

Due to the low iron content of Mercury's crust, spectral absorption bands normally used to map the mineral composition of a planetary surface are absent. For this reason, a principal component analysis of the three-color MDIS basemap is employed to allow a first-order mapping of compositional differences (Chabot et al., 2016; Klima et al., 2018; Murchie et al., 2015; Robinson et al., 2008). Specifically, the first principal component of the three-color (430, 750, and 1,000 nm) basemap is assigned a green color, the second principal component is assigned red, and the 430/1,000-nm ratio is shown as blue. As described most recently by Klima et al. (2018), this approach produces several distinctive reflectance units. The reddish-brown areas on the mosaic typically represent high-reflectance plains (HRP), which are believed to be volcanic in origin and

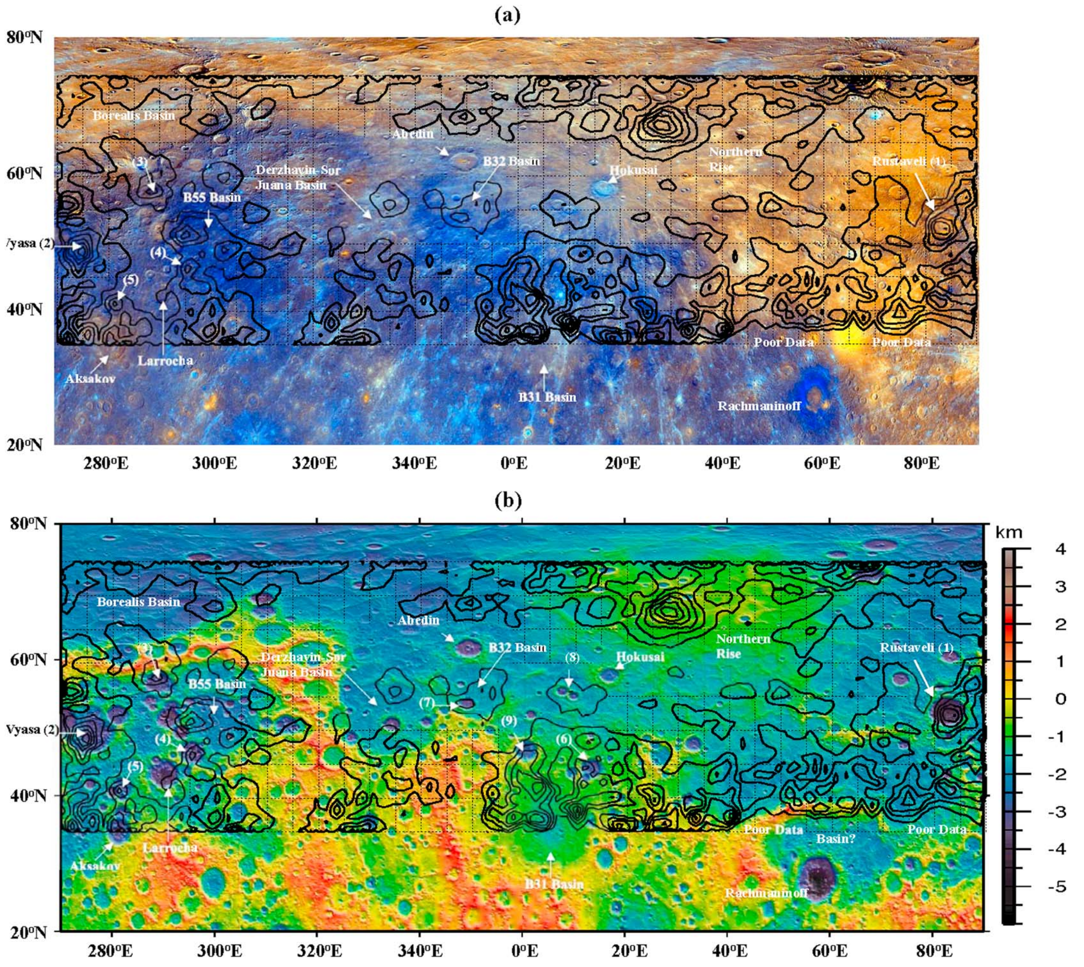

**Figure 3.** Superposition of the equivalent source dipole field magnitude at 40-km altitude (contour interval, 1 nT) onto: (a) a MESSENGER enhanced color image composite; and (b) a MErcury Surface, Space ENvironment, GEochemistry, and Ranging Laser Altimeter elevation map. See the text for further explanation.

are especially present in the northern lowlands and within Caloris (Denevi et al., 2013; Head et al., 2008, 2011). Bluish areas (low-reflectance blue plains [LBP]) indicate high ratios of reflectance at 430 nm relative to 1,000 nm. They consist at least partly of volcanic plains that are often more densely cratered, and thus older, than the HRP. The darkest blue areas represent low-reflectance material (LRM), consisting mainly of impact-mixed differentiated crust, including impact basin ejecta.

As noted by H16 for the mapped area on the Caloris side of Mercury, there is a tendency for weaker fields to occur over HRP (except within Caloris itself), especially over the northern lowlands, and for stronger fields to occur over LRM and LBP, especially that around Caloris. In Figure 3a, a similar tendency is present on the western side of the map with low fields in the volcanically resurfaced Borealis basin and higher fields southward of 60° N where LBP dominates. On the eastern side of the map, this tendency is less clear with strong anomalies over the northern rise (to be discussed below) and in the southeastern sector north of Rachmaninoff, both areas overlain by high-reflectance volcanic material. A strong anomaly occurs over Rustaveli crater whose interior contains HRP. This is similar to the interior of Caloris, which also contains strong anomalies. In all of these cases, it is possible that the anomaly sources consist of impact melt lying beneath a thin, poorly magnetic volcanic resurfacing layer.

Comparisons can also be made with geologic maps, which can reveal ancient structures and relative age relationships not visible on topographic or reflectance maps. Figure 4a is a superposition of the field magnitude map of Figure 2b onto a digital composite of geologic maps at a scale of 1:3M (Galluzzi et al., 2016; Wright et al., 2018a). As described in the latter references, digital compositing at this scale of published geologic maps is an ongoing project in support of the upcoming BepiColombo mission jointly conducted by the European

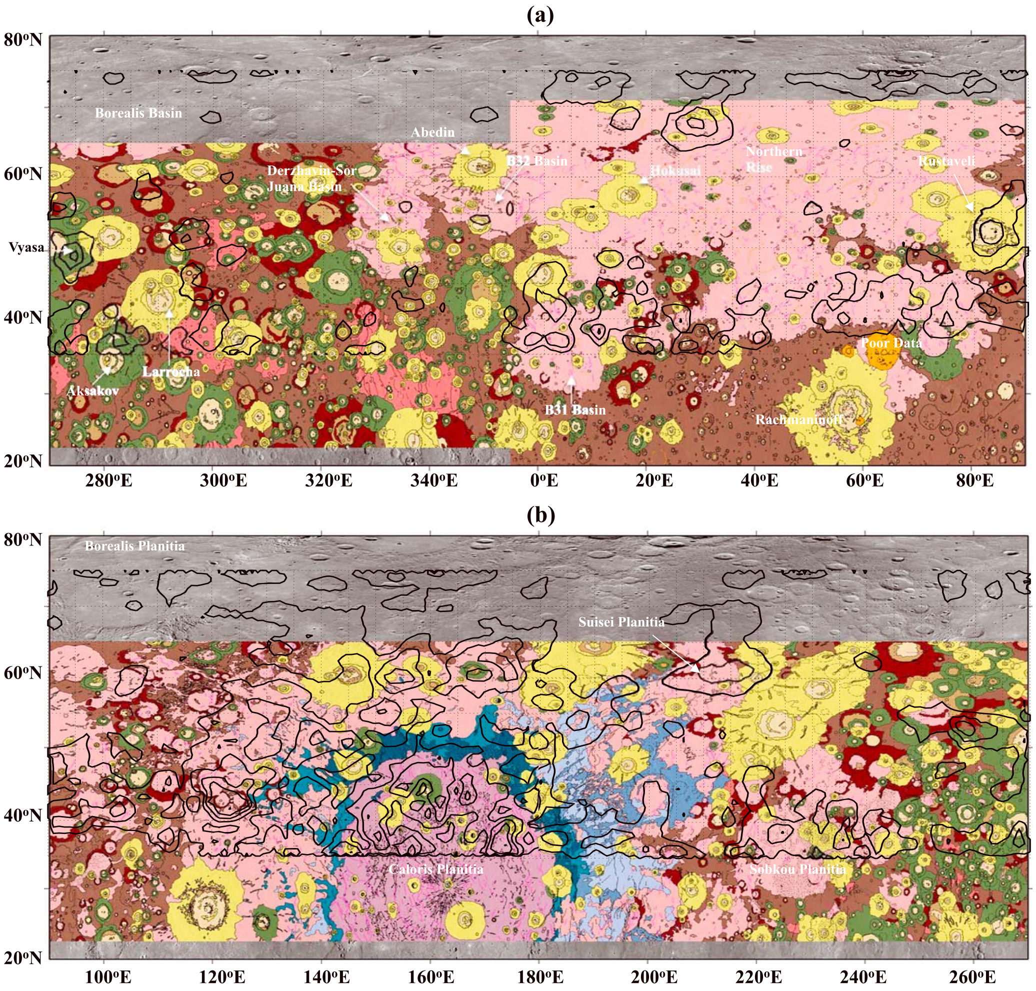

**Figure 4.** As in Figure 3 but superposed onto a composite of recently reconstructed geologic maps of Mercury (Galluzzi et al., 2018). (a) The same region as in Figure 3 using individual maps by Galluzzi et al. (2016) and Wright et al. (2018a); (b) the Caloris side mapped magnetically by H16 using geologic maps by Mancinelli et al. (2016) and Guzzetta et al. (2017). The contour interval in both maps is 2 nT.

Space Agency and the Japan Aerospace Agency. Figure 4b is a superposition of an updated version of the previous field magnitude map of H16 onto a similar composited geologic map of the Caloris side of Mercury (Guzzetta et al., 2017; Mancinelli et al., 2016). The updated version was produced from MESSENGER data after further editing to minimize downward continuation errors near the southern edge of the map, especially in and around Sobkou Planitia. The contour interval in Figure 4a is 2 nT to be consistent with the field map in Figure 4b. Comparing the field maps in Figures 4a and 4b, the much larger amplitude of anomalies within and around Caloris is evident. The yellow colors on both maps represent the freshest surfaces, consisting primarily of younger (Calorian period or younger) impact craters and surrounding ejecta fields, while green colors indicate moderately young craters and their ejecta. The darker brown unit in Figures 4a and 4b represents older-cratered terrain that has been heavily reworked by pre-Caloris impact events. The pink unit in Figure 4a represents younger volcanic plains (e.g., Head et al., 2011), while the darker red color indicates possible older volcanic plains. In Figure 4b, the magenta unit within Caloris represents volcanic plains emplaced at a time after the basin-forming impact. The dark blue unit adjacent to the Caloris rim is the Caloris Montes Formation, while the lighter blue unit is the Odin Formation (Guest & Greeley, 1983). The surfaces of both of these units consist at least partly of Caloris ejecta materials as confirmed by a recent study of circum-Caloris *knobs*, which are a distinctive feature of the Odin Formation (Wright et al., 2018b).

The extensive pink unit surrounding Caloris in Figure 4b represents smooth plains (spectrally blue in this region). Crustal fields are unusually strong over this unit, especially on the western side of Caloris. Both volcanic- and impact-related origins have been proposed for these smooth plains (Denevi et al., 2013). A volcanic origin is supported by evidence for continuity between the interior and exterior plains (Rothery et al., 2017) and by superposed crater size-frequency distributions, which indicate an age substantially younger than the Caloris interior plains and rim (Strom et al., 2008). However, crater-count age estimates can be biased if the exterior plains have different crater production or retention properties than the interior plains or the Caloris rim. If at least some exterior plains have an impact-related origin, then they would consist of finely divided *fluidized* ejecta deposited during a base flow surge immediately following the Caloris impact (see the discussion in Denevi et al., 2013). They would then be analogous to the lunar Cayley plains, which are known to be anomalously magnetic and have an impact-related origin as verified by direct sampling at the surface (see the discussion in H15 and H16).

Finally, to investigate deeper crustal magnetic field sources, comparisons with gravity anomaly maps can be useful. Figure 5a superposes the 40-km-altitude field magnitude map of the region mapped here onto a free air gravity anomaly map recently derived from MESSENGER radio tracking data (A. Genova, private communication, May, 2018). Figure 5b is a superposition of the field magnitude map of H16 onto a similar gravity anomaly map for the Caloris-facing hemisphere. As reported by Smith et al. (2012), the northern rise has a nearly uncompensated strong positive gravity anomaly (~150 mgal) centered near 33° E and 68° N. This nearly coincides with the broad magnetic anomaly peak over the northern rise in Figure 3b centered at about 28° E and 67° N. As Figure 4b shows, the northern rise lies entirely within, and is surfaced, by the vast extent of Mercury's northern smooth plains. Also, the size-frequency distributions of superposed craters on the rise are not significantly different from those of the surrounding northern lowlands. This would favor an internal origin for the rise, possibly involving mantle dynamic uplift occurring well after the volcanic resurfacing event (Zuber et al., 2012).

As seen in Figure 5b, the association of strong magnetic anomalies with strong positive free-air gravity anomalies is not limited to that over the northern rise. Strong and broad gravity anomalies are also found over the Caloris impact basin and Sobkou Planitia, which contains an older impact basin. Both of the latter basins have groups of strong magnetic anomalies near and within them (H16).

### 3.3. Correlations With Impact Craters and Basins

The strongest anomalies on the side mapped here (e.g., Figure 2c) have smoothed amplitudes at 40 km altitude of about 6 nT, somewhat less than those of the strongest anomalies within and near Caloris (~8 nT; H16). Some of the anomalies appear to be associated with impact basins and craters that are most easily seen on the topographic map of Figure 3b. A concentration of anomalies appears to be present over the mapped part of the lava-filled B31 basin (diameter, 770 km, centered near 4° E and 37° N; Fassett et al., 2012). This group of anomalies has amplitudes up to ~5 nT and extends northward up to about 50° N. It is distinct from the east-west belt of anomalies that continues to 90° E because anomalies are weak at 30° E to 40° E. It has many similarities to the anomaly groups near Caloris and Sobkou, but confirmation of a real association with B31, like Sobkou, must await future measurements at lower latitudes. With respect to other basins, it is clear that only weak anomalies are found in the probable Derzhavin-Sur Juana basin (580 km in diameter, centered at 332° E and 52° N) and the probable B32 basin (370 km in diameter, centered at 349° E and 56° N). The latter two basins as well as B31 and Sobkou have been degraded by later impacts and are relatively ancient (Tolstojian or pre-Tolstojian). It is possible that their associated anomaly sources have been weakened by impact shock demagnetization.

The source of anomalies in the belt extending from about 40° E to 90° E in the southern part of the map is very uncertain. On the one hand, it could be speculated that these anomalies are distributed roughly circumferential to an unnamed quasi-circular feature with a possible partial outer rim visible in the topography centered at about 60° E and 32° N (labeled "Basin?" in Figure 3b). On the other hand, this belt of anomalies also occurs near the largest pyroclastic deposit on the planet (bright yellow area near 60° E and 35° N in Figure 3a, recently named Nathair Facula; see also Figure 7b) and over a smaller example (Neidr Facula) to the west (Thomas et al., 2014; Weider et al., 2016). This might suggest volcanic intrusions as sources. However, the spacecraft altitude was too high directly over these features to allow reliable mapping. Also, as was found for the Caloris side of Mercury, only relatively weak anomalies are present over the northern lowlands, most of which has been volcanically resurfaced (Denevi et al., 2013; Head et al., 2011). Thus, evidence for volcanic sources on Mercury remains uncertain.

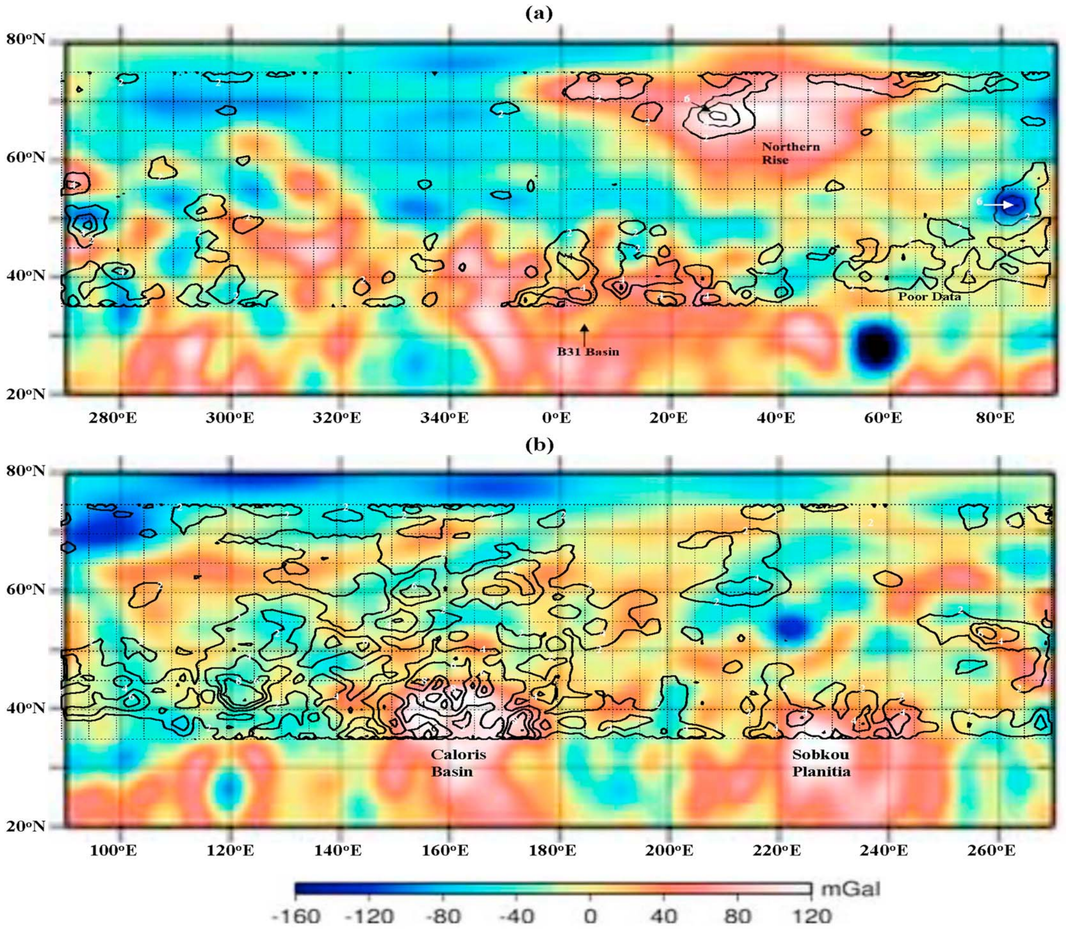

**Figure 5.** As in Figure 4 but superposed onto a MESSENGER radio tracking free-air gravity anomaly map (A. Genova, private communication, 2018).

As seen in Figure 3b, two of the three strongest isolated anomalies (amplitudes ~6 nT; labeled (1) and (2)), are located over two of the largest craters that are easily visible in the topography, that is, with very low-lying floors: Rustaveli (~200 km in diameter, centered at 83° E and 52° N) and Vyasa (~300 km in diameter, centered at 275° E and 50° N). As seen in Figure 4a, Rustaveli is relatively young, while Vyasa is relatively old and is largely overlain by ejecta deposits from the nearby younger craters, Stravinski (170 km in diameter; 281° E

**Table 1**
*Possible Impact Crater—Magnetic Anomaly Associations* [a]

| # | Name[b] | Center location | Approximate diameter (km) | Anomaly strength (nT) | Peak location |
|---|---|---|---|---|---|
| (1) | Rustaveli | 83°E, 52°N | 200 | 6 | 84°E, 52°N |
| (2) | Vyasa | 275°E, 50°N | 300 | 6 | 275°E, 49°N |
| (3) | — | 289°E, 57°N | 136 | 3 | 288°E, 58°N |
| (4) | — | 295°E, 46°N | 136 | 3 | 295°E, 46°N |
| (5) | — | 282°E, 41°N | 128 | 4 | 281°E, 41°N |
| (6) | — | 13°E, 44°N | 145 | 3 | 12°E, 45°N |
| (7) | — | 349°E, 53°N | 77 | 2 | 349°E, 53°N |
| (8a) | — | 8°E, 55°N | 64 | 2 | 9°E, 56°N |
| (8b) | — | 10°E, 55°N | 50 | 2 | 9°E, 56°N |
| (9) | Sousa | 1°E, 47°N | 138 | 3 | 1°E, 46°N |

[a] Listed in order of increasing uncertainty. [b] If any.

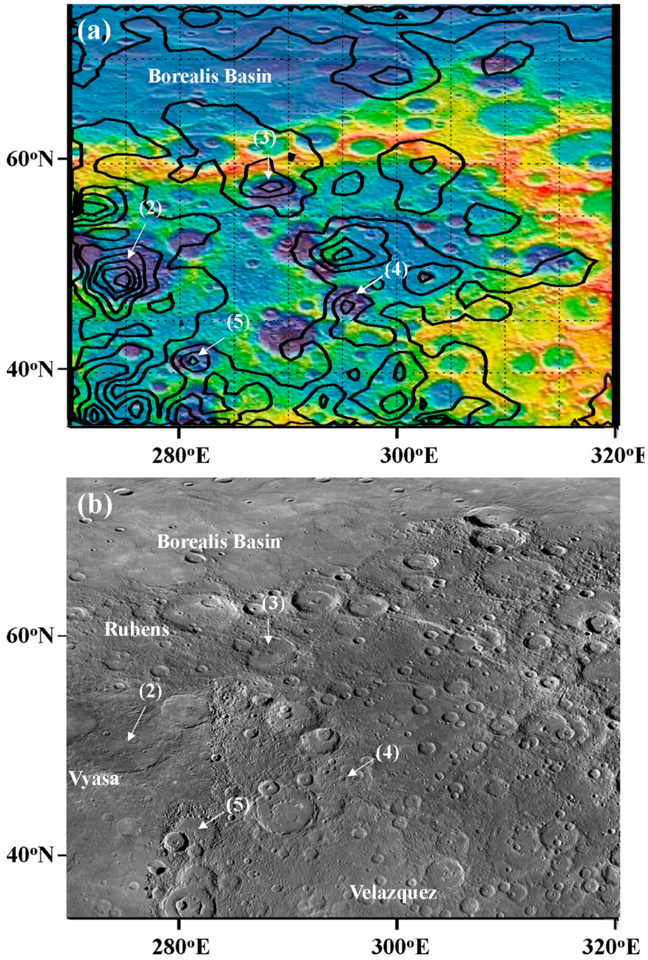

**Figure 6.** (a) Western section of Figure 3b (270° E to 320° E); (b) corresponding section of a MESSENGER monochrome mosaic (see the text). The locations of magnetic anomalies that fall within degraded older craters identifiable on the topographic map are indicated by numbers.

and 52° N) and Sholem Aleichem (190 km in diameter; 269.5° E and 51° N). Only one other crater lying fully in the mapped region, Larrocha (196 km in diameter, centered at 290° E and 43° N; similar in age to Rustaveli) is comparable in size to Rustaveli and Vyasa and is clearly visible in the topography. No distinct anomaly is associated with Larrocha. Also, several other smaller young craters (e.g., Abedin and Hokusai, 116 and 114 km in diameter, respectively) have no associated anomalies.

Rustaveli is younger than the Borealis plains and is among the youngest large craters on Mercury (Ostrach et al., 2015; Wright et al., 2016). The interior fill material could in principle be either impact melt or volcanic lava. The absence of flooded or "ghost" craters on the floor suggests emplacement soon after formation of the crater, which would be consistent with impact melt. However, the incomplete visibility of its central peak ring suggests that the volume of fill material is too large to be impact melt. Therefore, a volcanic lava origin is favored, which would be consistent with the presence of HRP in its interior, as noted in section 3.2.

The probability that two of the three strongest anomalies in the mapped area would by chance have maxima lying within two of the three largest impact craters visible in the topography can be estimated conservatively as follows. First, the probability that any single anomaly peak would fortuitously lie within a given crater is $A_c/A_m$, where $A_c$ is the area of the crater and $A_m$ is the mapped area. The mapped area (35° N to 75° N, 180° of longitude) is approximately $1.5 \times 10^7$ km$^2$. For Rustaveli, $A_{c1} \simeq 3.1 \times 10^4$ km$^2$; for Vyasa, $A_{c2} \simeq 7.1 \times 10^4$ km$^2$; and for Larrocha, $A_{c3} \simeq 3.0 \times 10^4$ km$^2$. The probability that one of the three strongest anomaly peaks would fall within Rustaveli is therefore roughly $3 \times A_{c1}/A_m \simeq 0.6\%$. The probability that one of the three would fall within Vyasa is about 1.4%. The probability that two of the three would fall within any of the three craters can be estimated as $3/2 \times (A_{c1} + A_{c2} + A_{c3})/A_m \simeq 1.3\%$. The correlation of strong anomalies with large impact craters seen in Figure 3b therefore likely implies a physical relationship rather than a chance occurrence.

As listed in Table 1 and shown in more detail in Figures 6, 7, and 8, it is possible that other impact craters within the mapped region are associated with magnetic anomalies of intermediate amplitude. The remaining labels (3)–(9) in Figure 3b identify these seven other candidates. While many of these possible associations are uncertain, they are listed here in approximate order of increasing uncertainty to motivate future tests using either new orbital data or existing MESSENGER magnetometer data from earlier time periods.

Figure 6 compares a section of Figure 3b with a MESSENGER monochrome mosaic. Note that the entire mosaic is at 166 m per pixel resolution, but a section near the southwestern edge, including Vyasa crater, is less clear because it was imaged at a lower solar-zenith angle so there are fewer shadows. In addition to the 6-nT anomaly within Vyasa, a ~3-nT anomaly peak, labeled (3), lies within an older ~136-km-diameter crater centered near 289° E and 57° N. Another ~3-nT anomaly peak, labeled (4), lies within a degraded older crater of about the same size centered at 295° E and 46° N. This crater is identifiable in the topography but contains superposed smaller craters and is less visible in the imagery. Finally, a ~3-nT anomaly peak, labeled (5), lies within an older ~128-km-diameter crater centered at 282° E and 41° N. On the other hand, a 4-nT anomaly at 295° E and 51° N is not clearly associated with any crater although it lies just within a "suggested" B55 basin, centered at 300° E and 53° N (Fassett et al., 2012).

The probability that four of the five strongest anomaly peaks within the mapped area of Figure 6 would by chance lie within impact craters with diameters greater than about 100 km can be estimated in the same way as described above. Not counting Aksakov, which lies near the poorly mapped southern boundary, but including Sholem Aleichem, which lieson the western boundary, there are about 10 impact craters with diameters

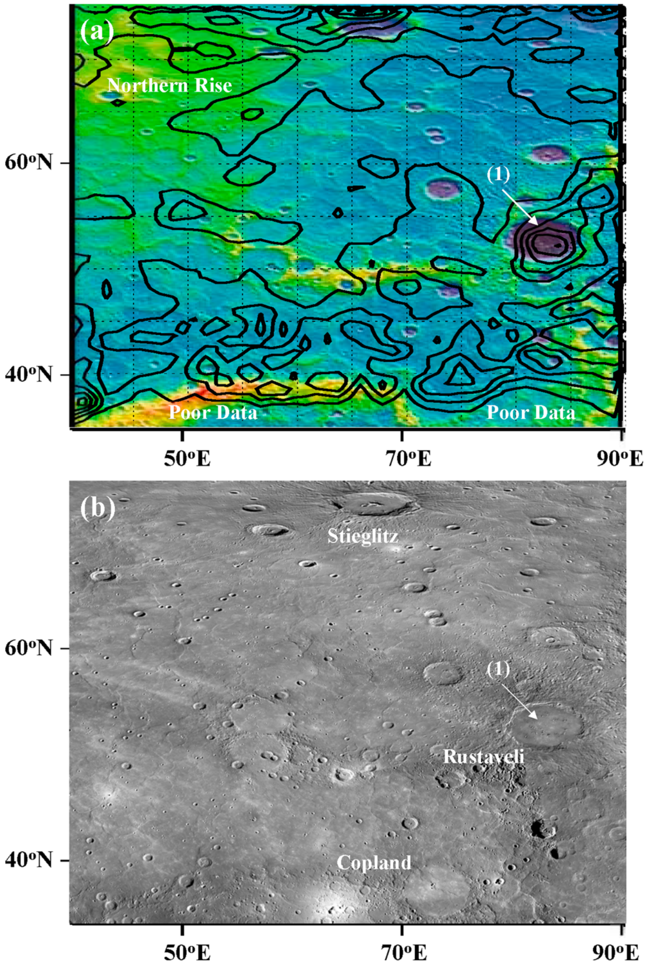

**Figure 7.** As in Figure 6 but for the eastern section of Figure 3b (40° E to 90° E). The anomaly designated (1) falls within the relatively young Rustaveli crater (~200 km in diameter).

ranging from 100 to 300 km with sufficiently large depths that they are easily visible in the topography within the boundaries of Figure 6. (Note that some craters at high latitudes may appear to be larger than 100 km in east-west dimension because of the cylindrical map projection.) The total surface area is $A_m \sim 4 \times 10^6$ km$^2$. The probability that one of the five anomaly peaks would lie within Vyasa is $5 \times A_{c2}/A_m \simeq 9\%$. The probabilities that one of the five would lie within the craters labeled (3), (4), and (5) are about 1.7%, 1.7%, and 0.8%, respectively. Assuming a mean diameter of about 150 km for the remaining six craters, the total area of the 10 craters is $A_{ct} \sim 2.2 \times 10^5$ km$^2$. The probability that four of the five would lie by chance within any of the 10 impact craters in this diameter range identifiable in the topography is roughly $5/4 \times A_{ct}/A_m \simeq 7\%$. The apparent preference for associations with deeper impact craters is discussed further in section 5 below.

Figure 7 shows a comparison in the same format as Figure 6 for the eastern part of the mapped area. Rustaveli and Steiglitz (100 km in diameter) are clearly visible in the topography. The Rustaveli anomaly is centered within the crater (Table 1), while other smaller craters have no associated anomalies. A strong anomaly is located just northwest of Steiglitz (see section 5 for further discussion of this anomaly). Copland is comparable in size to Rustaveli but is not prominent in the topography. It lies near the southern boundary where mapping is less reliable and no distinct anomaly is associated with this crater.

Figure 8 shows a comparison in the same format for the central part of the mapping area. While no anomaly is clearly associated with any impact crater in this region, some possible associations can be noted. Specifically, one 3-nT anomaly, labeled (6), could be associated with an unnamed ~130-km-diameter crater centered at 13° E and 44° N. Also, a 2-nT anomaly could be associated with the ~77-km-diameter crater, labeled (7), centered at 349° E and 53° N. An elongated anomaly with a peak amplitude of 2 nT (labeled (8)) could be associated with a pair of smaller craters listed as 8a and 8b in Table 1. Finally, contours are elongated suggesting a possible anomaly over the ~138-km-diameter crater Sousa (labeled (9); centered at 1° E and 47° N).

As seen in Figure 3b, crater-associated anomalies are found mainly near the western and eastern boundaries of the map at 270° E and 90° E. It is noteworthy that these longitudes are also where solar insolation combined with Mercury's 3:2 spin-orbit resonance leads to a less heated surface and subsurface. However, it is unlikely that the resulting longitudinal temperature variation is sufficient to suppress anomalies at 0° E. According to detailed thermal models by Vasavada et al. (1999), at 55° N, the maximum daily surface temperature at 0° E and 180° E longitude approaches 600 K but remains constant at ~400 K at depths of half a meter or more. At 270° E and 90° E, the surface temperature at the same latitude peaks at ~500 K but remains constant at about 300 K at depth. Since Mercury's crustal magnetic sources are more than 0.5 m below the surface, the relevant longitudinal temperature variation is ~300 to 400 K. In contrast, the Curie temperature of metallic iron-nickel alloys ranges from about 820 to 1,040 K (e.g., Rochette et al., 2008), so the temperature variation should have little effect on these carriers. Even if pyrrhotite ($Fe_{(1-x)}S$) is the dominant carrier, the Curie temperature would range from 560 to 590 K and so should be little affected by the solar-induced temperature variation. Empirical support for this conclusion is provided by the fact that anomalies are strong within Caloris, which is centered near one of the longitudes of maximum surface temperature.

## 4. Discussion

### 4.1. Possible Origins of Crater-Associated Anomalies

The association of magnetic anomalies with some impact basins/craters but not others represents a new constraint on crustal magnetic sources at Mercury. In this section, possible explanations for this observation are

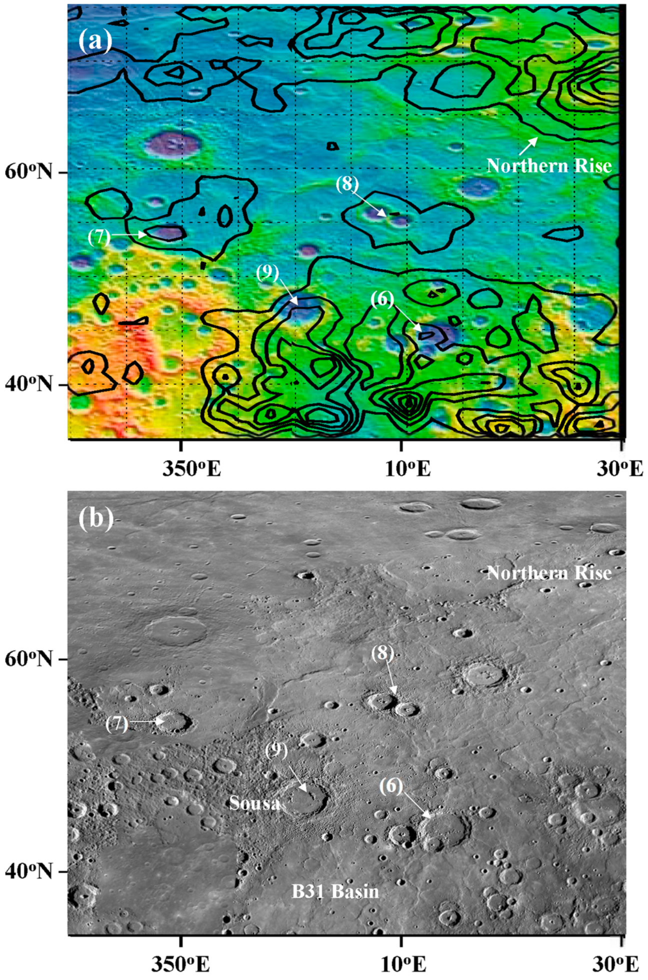

**Figure 8.** As in Figures 6 and 7 but for the central part of Figure 3b (340° E to 30° E). The possible associations of numbered anomalies with craters are discussed in the text.

discussed. Impact crater calculations are then carried out to allow a more quantitative investigation in the final subsection of an impactor-related origin and whether the observed anomalies are likely to be remanent or induced.

Because Mercury has some similarities to the Moon (heavily cratered surface, reducing geochemical conditions), some aspects of lunar observational evidence should be considered. In particular, anomalies are observed within a number of Nectarian-aged lunar impact basins such as Crisium, Moscoviense, and Leibnitz (Halekas et al., 2003; Hood, 2011; Kim et al., 2015; Oliveira et al., 2017; Tsunakawa et al., 2015). Weaker anomalies within the Imbrian-aged Schrödinger and Imbrium basins have also been identified (Hood & Spudis, 2016). Because these basin/crater interiors were heated to high temperatures and cooled below the metallic iron Curie temperature over a long time period (>$10^4$ years), a long-lived, steady magnetizing field is implied. The combination of both sample and orbital results has led to the now generally accepted conclusion that an ambient core dynamo field existed during early lunar history (for a review, see Weiss & Tikoo, 2014).

Some groups have suggested igneous sources of lunar anomalies consisting of vertical tabular (dike) intrusions (Hemingway & Tikoo, 2018; Purucker et al., 2012; Tsunakawa et al., 2014, 2015) while other groups have suggested sources in the form of impact basin ejecta deposits (Hood et al., 2013; Wieczorek et al., 2012). Analyses of Apollo samples found that impact melt rocks originating from large basin-forming impacts contain enhanced metallic iron abundances (1–2 wt %) that were apparently derived from the impactors that formed the basins (Haskin et al., 1998; Korotev, 1994, 2000). Independent magnetic analyses of impact breccias further showed that their enhanced metallic iron contents (and resulting stronger magnetization intensities) are at least partly of meteoritic origin (Rochette et al., 2010).

After more accurate lunar topographical mapping during the 1990s combined with the availability of global Lunar Prospector magnetometer data in the early 2000s, it became clear that some of the strongest anomalies on the lunar far side are in an area along the northwest rim of the South Pole-Aitken (SPA) basin, which is the oldest and largest discernible lunar basin (Purucker et al., 2006; Richmond & Hood, 2008). It was subsequently proposed by Wieczorek et al. (2012) that many of these anomalies could be caused by magnetization of iron-enriched ejecta from the impact that produced SPA. Numerical simulations by the latter authors showed that, depending on the impact angle, substantial amounts of the iron core of an asteroid-sized impactor would be incorporated into impact melt deposited either within the basin or external to it. Thermoremanent magnetization (TRM) of this ejecta in the early core dynamo magnetic field could explain the observed anomalies.

Another variant of the impact ejecta source model supposes that younger impact basins are responsible for most strong lunar anomalies. Several anomalies on the near side (Reiner Gamma and Rima Sirsalis) are oriented approximately radial to the center of the Imbrium basin (Halekas et al., 2001). The strongest single nearside anomaly is near the Apollo 16 landing site over the Descartes mountains, which is interpreted as ejecta from either the Imbrium or Nectaris basin-forming impacts (Richmond et al., 2003). In addition to being peripheral to SPA, many farside anomalies are in areas that are approximately antipodal to the youngest large basins (Imbrium, Orientale, Serenitatis, Crisium, and Schrödinger; Hood et al., 2013; Mitchell et al., 2008). Numerical simulations show that concentrations of ejecta will occur antipodal to a basin-forming impact (e.g., Hood & Artemieva, 2008). If some ejecta deposits near a forming basin or antipodal to it contained more impactor-derived metallic iron than did other ejecta from the basin, strong anomalies would be expected.

Both the SPA ejecta and the younger basin ejecta models have an advantage in that the susceptibility of metallic iron-enriched ejecta to TRM is orders of magnitude larger than that of typical lunar igneous rocks such as mare basalt (Weiss & Tikoo, 2014). On the other hand, Hemingway and Tikoo (2018) have recently proposed that, under favorable conditions (high-temperature magmas in a highly reducing environment), dikes or lava tubes with thicknesses >1 km could acquire magnetization intensities consistent with observed magnetic anomaly amplitudes.

Since magnetic anomalies on Mercury are clearly associated with the Caloris impact basin and with at least two sizeable craters, Vyasa and Rustaveli, it is possible that these anomalies are also a consequence of iron-enriched impact ejecta. In this interpretation, the absence of anomalies within some impact craters/basins would be due to either (a) a near absence of iron in the impactor (e.g., cometary nuclei impactors) or (b) an oblique impact angle (<45°), which would have deposited iron-rich ejecta only outside of the craters/basins (Wieczorek et al., 2012).

Present-day impact velocities of asteroidal or cometary bodies on Mercury are typically 20 to 50 km/s (Le Feuvre & Wieczorek, 2011), which is a factor of about two larger than typical lunar impact velocities. Velocities may have been somewhat reduced at early times when planetesimals were forming due to collisional or gravitational (near-miss) friction. We therefore consider a range of possible impact velocities between 20 and 40 km/s. For a given impact angle and velocity, the impactor size and density required to produce a crater of a given diameter depend on both the density and nature of the target material (unconsolidated or solid) and on the strength of the planetary gravity field. The gravitational acceleration and crustal mean density at Mercury are known to be 3.7 m/s$^2$ and 3,200 kg/m$^3$, respectively (Smith et al., 2012). We consider two extreme end members of target material, equivalent to loose sand and competent rock. These likely bracket the true strength of Mercury's upper crust, which, like the lunar upper crust, is in the form of a megaregolith. Although the metallic iron content of likely impactors during Mercury's early history is difficult to estimate, some guidance is provided by meteoritic compositions. The metallic iron contents of ordinary and carbonaceous chondrites are in the range of 18–28 and 19–24 wt %, respectively, while iron meteorites consist mostly of Fe (Jarosewich, 1990). At the other extreme, an ice-rich cometary impactor could be nearly devoid of metallic iron. For a given impact mass density, the impactor diameter needed to produce a crater of a given size can be estimated assuming Pi-group scaling (see, e.g., Melosh, 1989, chapter 7). A convenient online program for carrying out these calculations is available at www.eaps.purdue.edu/impactcrater (H. J. Melosh, private communication, May, 2018).

Tables 2 and 3 list the diameters of iron-enriched impactors that would produce a 200-km-diameter crater such as Rustaveli on Mercury for the stated ranges of impactor velocity and impact angle and for the two crustal consolidation end members (loose sand and competent rock). Table 2 considers the case of a pure metallic Fe impactor, while Table 3 considers a chondritic impactor containing 25 wt % metallic Fe. As seen in Table 2, for impact angles from the horizontal that would lead to deposition of most of the impactor iron within the crater (60° or more), the required impactor diameters are between 8.2 and 11.4 km for a loose sand target and between 3.75 and 5.9 km for a competent rock target. For a more realistic target hardness that is intermediate between loose sand and competent rock, impactor diameters would be in the range of ~6 to 9 km. Taking 10 km as an upper bound on the pure Fe impactor diameter, a total added mass of iron of no more than about $4 \times 10^{15}$ kg is implied. As seen in Table 3, for the same range of impact angles and velocities, required chondritic impactor diameters are between 11.5 and 16 km for a loose sand target and between 5.4 and 8.5 km for a competent rock target. The corresponding mean range is ~8 to 12 km. Taking 13 km as an upper bound on the impactor diameter together with a chondritic metallic iron volume fraction of ~10%, a total added mass of iron of no more than about $9 \times 10^{14}$ kg is implied. An ice-rich (cometary nucleus) impactor would add almost no metallic iron.

We next ask what volume of impact melt would be needed to produce a significant enhancement of the metallic iron concentration in the interior subsurface of Rustaveli if all of the allowed impactor iron is added to that volume. The mean surface concentration of iron on Mercury has been estimated from MESSENGER gamma-ray and X-ray measurements to be 1.5 to 2.0 wt % (Evans et al., 2012; Weider et al., 2014, 2015). This is the total Fe content (metallic plus that in silicates, oxides, and sulfides). However, because of the very reducing conditions during its formation, iron oxides and iron silicates are nearly absent on Mercury (e.g., Murchie et al., 2015). The measured Fe weight percent is therefore representative of the metallic Fe or Fe–Ni plus FeS content. Based on normative mineralogy calculations, most of the observed surficial Fe may be in the form of nonmagnetic iron sulfides (L. Nittler, private communication, May, 2018).

**Table 2**
*Pure Fe Impactor Required to Produce 200-km Crater* [a]

| Impact angle | Impact velocity (km/s) | Impactor diameter (km) Loose sand [b] | Impactor diameter (km) Competent rock [b] |
|---|---|---|---|
| 90° | 40 | 8.2 | 3.75 |
| 90° | 30 | 9.2 | 4.4 |
| 90° | 20 | 10.8 | 5.6 |
| 60° | 40 | 8.7 | 4.0 |
| 60° | 30 | 9.7 | 4.7 |
| 60° | 20 | 11.4 | 5.9 |
| 45° | 40 | 9.4 | 4.4 |
| 45° | 30 | 10.7 | 5.1 |
| 45° | 20 | 12.4 | 6.5 |
| 30° | 40 | 10.8 | 5.1 |
| 30° | 30 | 12.1 | 6.0 |
| 30° | 20 | 14.2 | 7.5 |

[a] Calculated using Pi-group scaling for a projectile density of 7,870 kg/m$^3$, a target density of 3,200 kg/m$^3$, and a gravitational acceleration of 3.7 m/s$^2$. [b] Assumed target type.

If we take a 4.0 wt% (1.8 vol%) enrichment of metallic iron (doubling of the mean crustal weight percent of Fe in any form) as being significant, then if the $4 \times 10^{15}$-kg-allowed mass of the pure iron impactor is added to a volume of impact melt, the implied volume is about $2.9 \times 10^{13}$ m$^3$, equivalent to a sphere of radius 19 km. If the impact melt is distributed in a cylindrical pool with diameter 100 km (comparable to the wavelength of the Rustaveli anomaly), then a thickness of 3.7 km is required. Alternatively, if the $9 \times 10^{14}$-kg-allowed mass of iron from the chondritic impactor is added to the impact melt volume, the implied volume is about a factor of four less, equivalent to a sphere of radius 12 km. The thickness of the 100-km-diameter cylinder would be reduced to ~0.9 km.

### 4.2. Induced Versus Remanent Magnetization

It is important to evaluate whether Mercury's anomalies are induced or remanent for several applications. First, if anomalies are remanent, they provide information about the existence and strength of Mercury's dynamo field over time. Second, inversions of isolated, dominantly dipolar, remanent anomalies can yield paleomagnetic pole positions useful for evaluating past reorientations of the rotation axis (true polar wander).

**Table 3**
*Chondritic Impactor Required to Produce 200-km Crater* [a]

| Impact angle | Impact velocity (km/s) | Impactor diameter (km) Loose sand [b] | Impactor diameter (km) Competent rock [b] |
|---|---|---|---|
| 90° | 40 | 11.5 | 5.4 |
| 90° | 30 | 12.9 | 6.3 |
| 90° | 20 | 15.1 | 8.0 |
| 60° | 40 | 12.2 | 5.7 |
| 60° | 30 | 13.6 | 6.7 |
| 60° | 20 | 16.0 | 8.5 |
| 45° | 40 | 13.3 | 6.2 |
| 45° | 30 | 14.8 | 7.3 |
| 45° | 20 | 17.4 | 9.2 |
| 30° | 40 | 15.2 | 7.2 |
| 30° | 30 | 17.0 | 8.5 |
| 30° | 20 | 20.0 | 10.7 |

[a] Calculated using Pi-group scaling for a projectile density of 3,400 kg/m$^3$, a target density of 3,200 kg/m$^3$, and a gravitational acceleration of 3.7 m/s$^2$. [b] Assumed target type.

The induced versus remanent issue has previously been addressed by Johnson et al. (2015; see section 7 of their supplementary online material). Assuming that anomaly sources contain no more metallic iron than that allowed by MESSENGER gamma-ray and X-ray surface measurements (1.5 to 2.0 wt%), it was found that induced sources with reasonable volumes are unlikely to explain fully the amplitude of the observed crustal anomalies at the spacecraft altitude. In addition, no obvious variation of crustal anomaly amplitudes was identified due to changes in the background magnetic field strength caused by magnetospheric activity, as would be expected if anomalies were dominantly induced.

However, as discussed above, the discovery of anomalies that are associated with some impact craters/basins on Mercury combined with available lunar evidence raises the possibility that subsurface iron concentrations are enhanced within these craters/basins over that allowed by surface gamma-ray and X-ray measurements. A new evaluation of induced versus remanent origins is therefore needed, taking into account the possible addition of impactor iron. A direct evaluation of whether individual impacted areas at northern midlatitudes are enhanced in Fe is not presently possible because Fe/Si elemental weight ratios on Mercury's surface derived from MESSENGER X-Ray Spectrometer data were possible only in the southern hemisphere (Weider et al., 2015). Even if these data were available for the northern hemisphere, as discussed in section 3, the interiors of craters such as Rustaveli may have been volcanically resurfaced, precluding a direct evaluation. However, using the limits on added metallic iron calculated in the previous subsection, it is possible to estimate theoretically the maximum expected induced field amplitude over Rustaveli.

For this purpose, consider for simplicity a homogeneous spherical source body in the presence of an arbitrarily oriented applied magnetic field, $\mathbf{B}_\circ = \mathrm{B}_\circ \hat{q}$. As shown in Appendix A, the vector magnetic anomaly due to such a body is given by

$$\mathbf{B}' = B_\circ [2\alpha (a/r)^3 \cos\theta \, \hat{r} + \alpha (a/r)^3 \sin\theta \, \hat{\theta}], \tag{1}$$

where $r$ is radial distance from the center of the source body with radius $a$, $\hat{r}$ is the corresponding unit vector, $\theta$ is colatitude measured from the direction of the applied field, $\hat{q}$, $\hat{\theta}$ is the corresponding unit vector, and

$$\alpha = \frac{\frac{\mu}{\mu_\circ} - 1}{\frac{\mu}{\mu_\circ} + 2}, \tag{2}$$

where $\mu$ is the permeability of the body, and $\mu_\circ$ is the permeability of free space. The susceptibility of the body, $\chi$, is defined as $\chi = \frac{\mu}{\mu_\circ} - 1$ (meter-kilogram-second or international system units) so that $\alpha = \chi/(\chi + 3)$. Metallic Fe−Ni alloys and one type of iron sulfide (pyrrhotite) are among the most likely magnetic phases in the reducing Mercury environment. The magnetic susceptibility of metallic Fe−Ni is in general a nonlinear function of the applied field strength (e.g., Jackson, 1975, chapter 5) but approaches a constant *low-field* value (for field strengths less than about 5,000 nT) of about $380 \times 10^{-6}$ $\mathrm{m^3/kg} \times 7{,}870$ $\mathrm{kg/m^3} \simeq 3$ (e.g., Rochette et al., 2008). This value is in agreement with that used by Johnson et al. (2015).

Consider a spherical source body with 4 wt% of added iron from a pure iron impactor sufficient to produce a 200-km crater such as Rustaveli on Mercury, resulting in $\chi = 0.054$ and $\alpha = 0.02$. As found in the previous subsection, such a source body would have a maximum radius of 19 km. At 50° N, the Mercury core dynamo field is directed mainly downward with an amplitude of 300 to 500 nT (e.g., Anderson et al., 2012). Substituting into (1) with $a = 19$ km and $\mathbf{B}_\circ = -(400\ \mathrm{nT})\,\hat{r}$, the maximum radial component anomaly for such a body with this Fe weight percent at a spacecraft altitude of 40 km is about −0.5 nT, which is much less than the radial component peak amplitude of the Rustaveli anomaly seen on orbit passes of (approximately −6 nT). This conclusion is not very sensitive to the assumed spherical geometry of the source. Also, if more than 4.0 wt% of Fe is considered to represent a significant iron enhancement, then the volume of the resulting source body is reduced, which causes the anomaly amplitude to fall off more rapidly with altitude.

From these calculations, which are based on the assumption that crater-associated anomalies are caused by added metallic iron from the impactor that produced the crater, it is concluded that the induced contribution to the Rustaveli anomaly and, by extension, other crater-associated anomalies must be very small. An upper limit is 0.5 nT (8% of the observed amplitude). In contrast, deposition within the transient impact cavity of a relatively thin layer (a few kilometers thick or less) of melt material containing the added metallic iron could have led to the formation of strong remanent anomalies via TRM (Johnson et al., 2015). This is especially true if Mercury's core dynamo field was stronger in its early history than it is today.

## 5. Summary and Further Discussion

Crustal field mapping presented here of the northern midlatitude region in the 90° W to 90° E longitude sector both augments previous results for the Caloris side (e.g., H15 and H16) and adds new information useful for understanding crustal magnetic sources on Mercury.

As described in section 3.3, a possible concentration of anomalies is found over the mapped part of the B31 basin (Figures 3 and 4a). If a true association with this basin is confirmed by future measurements at lower latitudes, then at least three impact basins (Caloris, Sobkou, and B31) would be known to have concentrations of anomalies. However, other basins (e.g., Borealis and Derzhavin Sur Juana) have either no anomalies or very weak anomalies.

In addition, strong anomaly peaks are found within the rims of the relatively young, 200-km-diameter crater Rustaveli and the much older 300-km-diameter large crater or small basin, Vyasa. This correlation has a very small (<2%) probability of happening by chance. Several smaller impact craters on the western side of the map also have anomaly peaks within their rims, while possible associations are noted for a number of others (Table 1). On the other hand, many impact craters have no obvious related anomalies.

As discussed in section 4.1, a possible interpretation of the observed correlation of magnetic anomalies with some impact craters/basins but not others is that some impactors delivered more ferromagnetic material (i.e., metallic Fe–Ni) to the interior subsurfaces and ejecta fields of the craters/basins that they produced. This interpretation is based partly on lunar observational evidence for magnetic anomalies within some impact basins (Halekas et al., 2003; Hood, 2011; Hood & Spudis, 2016) and for magnetic anomalies correlated with impact basin ejecta (e.g., Halekas et al., 2001; Hood et al., 1979; 2001; 2013). Theoretical models have been developed showing that ejecta from a basin-forming impact can be enriched in metallic iron from an impactor (Wieczorek et al., 2012) and concentrated antipodal to younger basins (Hood & Artemieva, 2008).

The absence of anomalies over some craters/basins on Mercury would, in this interpretation, be attributable to either an oblique impact angle, which would eject impactor iron well outside of the crater rim, or to an iron-depleted impactor (e.g., a basaltic achondrite with no metal or, in rare cases, a cometary nucleus). A possible example of an impact crater in the oblique impactor category is Stieglitz, which has an anomaly just outside its north rim (Figure 7). The absence of a magnetic anomaly near Hokusai is consistent with a suggestion that this very young (probably <100 Myr old) crater could be the site of a recent cometary impact that supplied Mercury's polar regions with more water ice than is currently found at the lunar poles (Ernst et al., 2018).

There is little evidence so far of an age dependence of craters or basins having associated magnetic anomalies on Mercury. Changes with time of the core dynamo magnetizing field intensity therefore do not provide a likely explanation for why some impact craters/basins have anomalies and others do not. For example, among impact basins, the Tolstojian or pre-Tolstojian Derzhavin-Sor Juana basin is nearly devoid of anomalies, while the comparably old Sobkou and B31 basins have anomaly concentrations. Although the anomalies within and around Caloris are stronger and more distinct than those near Sobkou and B31, this difference could reflect degradation of older basins and their associated anomalies with time rather than a stronger core dynamo field when Caloris formed.

The discussion of induced versus remanent origins of anomalies in section 4.2 generally agrees with the conclusion of Johnson et al. (2015) that present-day-induced fields are unlikely to be sufficient to explain the observed amplitudes of Mercury's stronger crustal magnetic anomalies, even if added iron from impactors is considered. The implied dominantly remanent origin of anomalies associated with impact craters on Mercury combined with the near certainty of a TRM origin of any magnetization within the crater rims means that they are good candidates for magnetic paleopole analyses.

With respect to anomalies outside of known impact basins and craters, comparisons with surface reflectance and geology generally support the tendency noted by H16 for only weak anomalies to occur over HRP material, which is believed to have a volcanic origin, while stronger anomalies are usually found over LRM and LBP (section 3). The comparison with geologic maps shows that the strongest anomalies outside of impact basins are found on the western side of Caloris over smooth plains units. The LRM and possibly some areas of the LBP are interpreted as volcanic material reworked by impact processes and overlain by impact ejecta containing carbon-rich material. An exception to this pattern is observed within some major basins and large craters (e.g., Caloris) whose interiors have been volcanically resurfaced but where strong anomalies are nevertheless found. In the latter cases, the stronger magnetic sources may consist of iron-enriched impact melt rocks beneath a veneer of poorly magnetized volcanic material.

Comparisons with a MESSENGER free-air gravity map (provided by A. Genova) in section 3 showed that a broad and strong magnetic anomaly over the northern rise nearly coincides with an areally extensive and strong free-air gravity anomaly (Figure 5a). Several other relatively strong and broad gravity anomalies are present over Caloris and Sobkou planitia, which also have groups of strong magnetic anomalies (Figure 5b). The northern rise consists of a region of internally generated uplift that postdates the formation of the northern lowlands (Klimczak et al., 2012; Zuber et al., 2012). Since there is little evidence for volcanic sources of magnetic anomalies elsewhere on Mercury, the occurrence of a strong and broad anomaly in this region is puzzling. As noted, for example, by James et al. (2015), large basin-forming impacts such as Caloris produce a thinner crust. It is therefore possible that a major impact may have preconditioned the region now occupied by the northern rise to a later mantle uplift event. If the impactor-added iron mechanism for the production of magnetic anomalies applies also to the northern rise anomaly, then the observed magnetic anomaly could be caused by the iron added during that early impact.

The possibility that impactor iron-enriched impact melt and ejecta are the sources of magnetic anomalies within and around Caloris and Sobkou raises the question of whether added impactor iron could contribute significantly to their observed free-air gravity anomalies. To test this hypothesis, limits on the added iron for a basin of known size could be estimated using the methods described in section 4.1. It may then be possible to model the resulting gravity anomaly contributions assuming that the distribution of the added iron correlates with that of the magnetic anomalies within and around the basin.

As noted in section 3, apparent associations of magnetic anomalies with impact craters are most easily identified on the topographic map of Figure 3b and are less visible on the MDIS image composite of Figure 3a. This suggests that crater depth could be a factor in determining whether a given crater has or does not have an associated magnetic anomaly. It might initially be thought that these crater-associated anomalies are simply a consequence of producing a cavity in a uniformly magnetized crust (Runcorn, 1975). However, a real planetary crust is seldom if ever magnetized uniformly due to compositional heterogeneity. Instead, magnetic anomalies are typically caused by magnetization contrasts rather than by topography in a uniformly magnetized spherical shell. If the apparent tendency for anomalies to be found within deeper craters is real, then an alternate possible explanation is that impactors dominantly made of iron impacting at a near-vertical angle would produce deeper craters than ordinary chondrite or cometary nucleus impactors.

Finally, although mapping of Mercury's crustal field using MESSENGER data covers only about 20% of the planet, results so far indicate that the association of magnetic anomalies with impact craters and basins is somewhat more prevalent on Mercury than on the Moon. This is true even though a lunar dynamo apparently existed during most of the lunar basin- and crater-forming era. One possible explanation is the stronger Mercury surface gravity field (2.2 times that of the Moon), which may have favored deposition of iron-rich impact melt and ejecta within and near a given crater rather than at larger distances. If this is the case, then concentration of iron-rich ejecta and magnetic anomalies at the antipodes of young impact basins may not have been as effective on Mercury as on the Moon. Future measurements by the BepiColombo mission and numerical simulations such as those of Wieczorek et al. (2012) using a stronger gravity field would assist in testing these possibilities.

## Appendix A

The following derivation follows those of Jackson (1975; Chapter 5), who considered a permeable spherical shell, and Dyal et al. (1976), who analyzed a multilayered permeable sphere. Consider a homogeneous spherical body of radius $a$ with uniform permeability $\mu$ exposed to an initially uniform and arbitrarily oriented magnetic field $\mathbf{H}_\circ = H_\circ \hat{q}$. In the absence of currents, $\mathbf{H} = -\nabla\Phi$, where $\Phi$ is a scalar potential. The magnetic induction $\mathbf{B} = \mu\mathbf{H}$ inside the sphere and $\mathbf{B} = \mu_\circ\mathbf{H}$ outside the sphere, where $\mu_\circ$ is the permeability of free space. Far from the sphere, $\mathbf{B} = B_\circ\hat{q} = \mu_\circ H_\circ \hat{q}$. For these conditions, $\nabla\cdot\mathbf{H} = 0$ at any location, and $\Phi$ satisfies Laplace's equation, $\nabla^2\Phi = 0$. The solution in spherical coordinates is derived, for example, in Jackson (1975, p. 84).

Outside the sphere ($r > a$),

$$\Phi(r,\theta) = -H_\circ r\cos\theta + \sum_{i=0}^{\infty} \frac{\alpha_i}{r^{i+1}} P_i(\cos\theta), \tag{A1}$$

where $\theta$ is colatitude measured from the applied field direction $\hat{q}$, $P_i$ is the Legendre polynomials of order $i$ in the variable $\cos\theta$, and $\alpha_i$ is undetermined scalar coefficients. Inside the sphere ($r < a$),

$$\Phi(r,\theta) = \sum_{i=0}^{\infty} \beta_i r^i P_i(\cos\theta), \tag{A2}$$

where $\beta_i$ are a second set of undetermined coefficients.

The boundary conditions are that the normal ($r$) component of **B** and the tangential component ($\theta$) of **H** are continuous at $r = a$. Applying these conditions and using $\mathbf{B} = -\mu_\circ\nabla\Phi$ for $r > a$, $\mathbf{B} = -\mu\nabla\Phi$ for $r < a$, and $P_1(\cos\theta) = \cos\theta$, it follows that all coefficients except for $\alpha_1$ and $\beta_1$ must be 0. The boundary conditions then lead to

$$\mu_\circ H_\circ a^3 + 2\mu_\circ\alpha_1 + \beta_1 a^3 = 0, \tag{A3}$$

and

$$-\alpha_1 + \beta_1 a^3 + H_\circ a^3 = 0. \tag{A4}$$

Eliminating $\beta_1$ between these two equations,

$$\alpha_1 = \frac{\mu - \mu_\circ}{\mu + 2\mu_\circ} H_\circ a^3. \tag{A5}$$

This can be rewritten in the form, $\alpha_1 = \alpha H_\circ a^3$, where

$$\alpha = \frac{\frac{\mu}{\mu_\circ} - 1}{\frac{\mu}{\mu_\circ} + 2}, \tag{A6}$$

which is the same as equation (2) in the text. Applying $\mathbf{B} = -\mu_\circ\nabla\Phi$ and defining the magnetic anomaly $\mathbf{B}' = \mathbf{B} - \mu_\circ\mathbf{H}_\circ$, then

$$\mathbf{B}' = B_\circ[2\alpha(a/r)^3\cos\theta\,\hat{r} + \alpha(a/r)^3\sin\theta\,\hat{\theta}], \tag{A7}$$

where $B_\circ = \mu_\circ H_\circ$, which is the same as equation (1) in the text.

**Acknowledgments**
Supported at the University of Arizona by grant 80NSSC17K0215 from the NASA Discovery Data Analysis Program. MESSENGER calibrated magnetometer data are available from the Planetary Plasma Interactions node of the NASA Planetary Data System (ppi.pds.nasa.gov). The MDIS-enhanced color mosaic used in the construction of Figure 3a was obtained from http://messenger.jhuapl.edu/Explore/Impages.html#global-mosaics. The background MLA elevation map used in Figure 3b was provided by G. Neumann and free-air gravity anomaly maps (one of which was used in Figure 5) were provided by A. Genova and M. Sori. Methods for carrying out the impact crater scaling calculations used in the production of Tables 2 and 3 were developed by H. J. Melosh and Ross Beyer (http://www.eaps.purdue.edu/impactcrater). We thank Jack Wright and Peter James for helpful comments. Paul Thomas and an anonymous reviewer provided useful criticisms that improved the quality of the final paper. Thanks again to the entire MESSENGER mission team for obtaining a remarkable data set.

## References

Anderson, B. J., Johnson, C., Korth, H., Winslow, R., Borovsky, J., Purucker, M., et al. (2012). Low-degree structure in Mercury's planetary magnetic field. *Journal of Geophysical Research*, *117*, E00L12. https://doi.org/10.1029/2012JE004159

Chabot, N. L., Denevi, B., Murchie, S., Hash, C., Ernst, C., Blewett, D., et al. (2016). Mapping Mercury: Global imaging strategy and products from the MESSENGER mission. Lunar and Planetary Science XLVII Abstract 1256.

Denevi, B., Ernst, C., Meyer, H., Robinson, M., Murchie, S., Whitten, J., et al. (2013). The distribution and origin of smooth plains on Mercury. *Journal of Geophysical Research: Planets*, *118*, 891–907. https://doi.org/10.1002/jgre.20075

Dyal, P., Parkin, C. W., & Daily, W. D. (1976). Structure of the lunar interior from magnetic field measurements. In *Proc. Lunar Sci. Conf. 7th*, Lunar and Planetary Institute, Houston (pp. 3077–3095).

Ernst, C. M., Chabot, N. J., & Barnouin, O. S. (2018). Could the Hokusai Impact have delivered Mercury's water ice? In *Mercury: Current and Future Science Abstract*, Lunar and Planetary Institute, Houston (6094 pp.).

Evans, L. G., Peplowski, P., Rhodes, E., Lawrence, D., McCoy, T., Nittler, L., et al. (2012). Major-element abundances on the surface of Mercury: Results from the MESSENGER gamma-ray spectrometer. *Journal of Geophysical Research*, *117*, E00L07. https://doi.org/10.1029/2012JE004178

Fassett, C. I., Head, J., Baker, D. M. H., Zuber, M., Smith, D., Neumann, G., et al. (2012). Large impact basins on Mercury: Global distribution, characteristics, and modification history from MESSENGER orbital data. *Journal of Geophysical Research*, *117*, E00L08. https://doi.org/10.1029/2012JE004154

Galluzzi, V., Guzzetta, L., Ferranti, L., Di Achille, G., Rothery, D. A., & Palumbo, P. (2016). Geology of the Victoria quadrangle (H02) Mercury. *Journal of Maps*, *12*(S1), 227–238.

Galluzzi, V., Guzzetta, L., Mancinelli, P., Giacomini, L., Lewang, A. M., Malliband, C., et al. (2018). The making of the 1:3M geological map series of Mercury: Current and future science 2018. Lunar and Planetary Institute, Houston, Abstract 6075, Abstract 1005.

Guest, J. E., & Greeley, R. (1983). *Geologic map of the Shakespeare Quadrangle of Mercury*. Arlington, VA: U.S. Geol. Surv. Map I-1408, U.S. Geol Surv.

Guzzetta, L., Galluzzi, V., Ferranti, L., & Palumbo, P. (2017). Geology of the Shakespeare Quadrangle (H03) Mercury. *Journal of Maps*, *13*(2), 227–238.

Halekas, J. S., Lin, R. P., & Mitchell, D. L. (2003). Magnetic fields of lunar multi-ring impact basins. *Meteoritics and Planetary Science*, *38*(4), 565–578.

Halekas, J. S., Mitchell, D. L., Lin, R. P., Frey, S., Hood, L., Acuña, M., & Binder, A. B. (2001). Mapping of lunar crustal magnetic fields using Lunar Prospector electron reflectometer data. *Journal of Geophysical Research*, *106*, 27,841–27,852.

Haskin, L. A., Korotev, R., Rockow, K., & Jolliff, B. (1998). The case for an Imbrium origin of the Apollo thorium-rich impact-melt breccias. *Meteorit Planetary Science*, *33*, 959–975.

Head, J. W., Chapman, C. R., Strom, R. G., Fassett, C. I., Denevi, B. W., Blewett, D. T., et al. (2011). Flood volcanism in the northern high latitudes of Mercury revealed by MESSENGER. *Science*, *333*, 1853–1856.

Head, J. W., Murchie, S. L., Prockter, L. M., Robinson, M. S., Solomon, S. C., Strom, R. G., et al. (2008). Volcanism on Mercury: Evidence from the first MESSENGER flyby. *Science*, *321*, 69–72.

Hemingway, D. J., & Tikoo, S. M. (2018). Lunar swirl morphology constrains the geometry, magnetization, and origins of lunar magnetic anomalies. *Journal of Geophysical Research: Planets*, *123*. https://doi.org/10.1029/2018JE005604

Hood, L. L. (2011). Central magnetic anomalies of Nectarian-aged lunar impact basins: Probable evidence for an early core dynamo. *Icarus*, *211*, 1109–1128.

Hood, L. L. (2015). Initial mapping of Mercury's crustal magnetic field: Relationship to the Caloris impact basin. *Geophysical Research Letters*, *42*, 10,565–10,572. https://doi.org/10.1002/2015GL066451

Hood, L. L. (2016). Magnetic anomalies concentrated near and within Mercury's impact basins: Early mapping and interpretation. *Journal of Geophysical Research: Planets*, *121*, 1016–1025. https://doi.org/10.1002/2016JE005048

Hood, L. L., & Artemieva, N. A. (2008). Antipodal effects of lunar basin-forming impacts: Initial 3D simulations and comparisons with observations. *Icarus*, *197*, 485–502.

Hood, L. L., Coleman Jr, P. J., Russell, C. T., & Wilhelms, D. E. (1979). Lunar magnetic anomalies detected by the Apollo subsatellite magnetometers. *Physics of the Earth and Planetary Interiors*, *20*, 291–311.

Hood, L. L., Richmond, N. C., & Spudis, P. D. (2013). Origin of strong lunar magnetic anomalies: Further mapping and examinations of LROC imagery in regions antipodal to young large impact basins. *Journal of Geophysical Research: Planets*, *118*, 1265–1284. https://doi.org/10.1002/jgre.20078

Hood, L. L., & Spudis, P. D. (2016). Magnetic anomalies in the Imbrium and Schrödinger impact basins: Orbital evidence for persistence of the lunar core dynamo into the Imbrian epoch. *Journal of Geophysical Research: Planets*, *121*, 2268–2281. https://doi.org/10.1002/2016JE005166

Hood, L. L., Zakharian, A., Halekas, J., Mitchell, D., Lin, R., Acua, M., & Binder, A. (2001). Initial mapping and interpretation of lunar crustal magnetic anomalies using Lunar Prospector magnetometer data. *Journal of Geophysical Research*, *106*, 27,825–27,839.

Jackson, J. D. (1975). *Classical electrodynamics* (2nd ed., 848 pp.). New York: John Wiley.

James, P. B., Zuber, M. T., Phillips, R. J., & Solomon, S. C. (2015). Support of long-wavelength topography on Mercury inferred from MESSENGER measurements of gravity and topography. *Journal of Geophysical Research: Planets*, *120*, 287–310. https://doi.org/10.1002/2014JE004713

Jarosewich, E. (1990). Chemical analysis of meteorites: Compilation of stony and iron meteorite analyses. *Meteoritics*, *21*, 1–22.

Johnson, C. L., Phillips, R. J., Purucker, M. E., Anderson, B. J., Byrne, P. K., Denevi, B. W., et al. (2015). Low-altitude magnetic field measurements by MESSENGER reveal Mercury's ancient crustal field. *Science*, *348*, 892–895.

Kim, H.-R., Hood, L., von Frese, R., & O'Reilly, B. (2015). Nectarian paleomagnetic pole inferred from Kaguya satellite magnetic observations of the central Leibnitz basin. Lunar Planet. Sci. XLVII Abstract 1914 Lunar and Planetary Institute, Houston.

Klima, R. L., Denevi, B. W., Ernst, C., Murchie, S., & Peplowski, P. (2018). Global distribution and spectral properties of low-reflectance material on Mercury. *Geophysical Research Letters*, 2945–2953. https://doi.org/10.1002/2018GL077544

Klimczak, C., Watters, T. R., Ernst, C. M., Freed, A. M., Byrne, P. K., Solomon, S. C., et al. (2012). Deformation associated with ghost craters and basins in volcanic smooth plains on Mercury: Strain analysis and implications for plains evolution. *Journal of Geophysical Research*, *117*, E00L03. https://doi.org/10.1029/2012JE004100

Korotev, R. L. (1994). Compositional variation in Apollo 16 impact-melt breccias and inferences for the geology and bombardment history of the Central Highlands of the Moon. *Geochimica et Cosmochimica Acta*, *58*, 3931.

Korotev, R. L. (2000). The great lunar hot spot and the composition and origin of the Apollo mafic ("LKFM") impact-melt breccias. *Journal of Geophysical Research*, *105*, 4317–4346.

Le Feuvre, M., & Wieczorek, M. (2011). Nonuniform cratering of the Moon and a revised crater chronology of the inner solar system. *Icarus*, *214*, 1–20.

Mancinelli, P., Minelli, F., Pauselli, C., & Federico, C. (2016). Geology of the Raditladi quadrangle, Mercury (H04). *Journal of Maps*, *12*(S1), 190–202.

Mayhew, M. A. (1979). Inversion of satellite magnetic anomaly data. *Geophysical Journal*, *45*, 119–128.

Melosh, H. J. (1989). *Impact cratering: A geologic process* (245 pp.). New York: Oxford University Press.

Mitchell, D. L., Halekas, J. S., Lin, R. P., Frey, S., Hood, L. L., Acua, M. H., & Binder, A. (2008). Global mapping of lunar crustal magnetic fields by Lunar Prospector. *Icarus*, *194*, 401–409.

Murchie, S. L., Klima, R. L., Denevi, B. W., Ernst, C. M., Keller, M. R., Domingue, D. L., et al. (2015). Orbital multispectral mapping of Mercury with the MESSENGER Mercury Dual Imaging System: Evidence for the origins of plains units and low reflectance material. *Icarus*, *254*, 287–305.

Oliveira, J. S., Langlais, B., Pais, M. A., & Amit, H. (2015). A modified equivalent source dipole method to model partially distributed magnetic field measurements, with application to Mercury. *Journal of Geophysical Research: Planets*, *120*, 1075–1094. https://doi.org/10.1002/2014JE004734

Oliveira, J. S., Wieczorek, M., & Kletetschka, G. (2017). Iron abundances in lunar impact basin melt sheets from orbital magnetic field data. *Journal of Geophysical Research: Planets*, *122*, 2429–2444. https://doi.org/10.1002/2017je005397

Ostrach, L. R., Robinson, M. S., Whitten, J. L., Fassett, C., Strom, R., Head, III, & Solomon, S. (2015). Extent, age, and resurfacing history of the northern smooth plains on Mercury from MESSENGER observations. *Icarus*, *250*, 602–622.

Parker, R. L. (1991). A theory of ideal bodies for seamount magnetism. *Journal of Geophysical Research*, *96*, 16,101–16,112. https://doi.org/10.1029/91JB01497

Purucker, M. E., Head III, J. W., & Wilson, L. (2012). Magnetic signature of the lunar South Pole-Aitken basin: Character, origin, and age. *Journal of Geophysical Research*, *117*, E05001. https://doi.org/10.1029/2011JE003922

Purucker, M., Sabaka, T., Halekas, J., Olsen, N., Tsyganenko, N., & Hood, L. (2006). The lunar magnetic field environment: Interpretation of new maps of the internal and external fields. Lunar Planet. Sci. XXXVI, Abstract 1933.

Richmond, N. C., & Hood, L. L. (2008). A preliminary global map of the vector lunar crustal magnetic field based on Lunar Prospector magnetometer data. *Journal of Geophysical Research*, *113*, E02010. https://doi.org/10.1029/2007JE002933

Richmond, N. C., Hood, L. L., Halekas, J. S., Mitchell, D. L., Lin, R. P., Acua, M., & Binder, A. B. (2003). Correlation of a strong lunar magnetic anomaly with a high-albedo region of the Descartes mountains. *Geophysical Research Letters*, *30*(7), 1395. https://doi.org/10.1029/2003GL016938

Robinson, M. S., Murchie, S. L., Blewett, D. T., Domingue, D. L., Hawkins III, S. E., Head, J. W., et al. (2008). Reflectance and color variations on Mercury: Regolith processes and compositional heterogeneity. *Science*, *321*, 66–69.

Rochette, P., Gattacceca, J., Bonal, L., Bourot-Denise, M., Chevrier, V., Clerc, J.-P., et al. (2008). Magnetic classification of stony meteorites: 2. Non-ordinary chondrites. *Meteoritics and Planetary Science*, *43*(Nr5), 959–980.

Rochette, P., Gattacceca, J., Ivanov, A., Nazarov, M., & Bezaeva, N. S. (2010). Magnetic properties of lunar materials: Meteorites, Luna and Apollo returned samples. *Earth Planet Science Letters*, *292*, 383–391.

Rothery, D. A., Mancinelli, P., Guzzetta, L., & Wright, J. (2017). Mercury's Caloris basin: Continuity between the interior and exterior plains. *Journal of Geophysical Research: Planets*, *122*, 560–576. https://doi.org/10.1002/2017JE005282

Runcorn, S. K. (1975). On the interpretation of lunar magnetism. *Physics of the Earth and Planetary Interiors*, *10*, 327–335.

Smith, D. E., Zuber, M., Phillips, R., Solomon, S., Hauck II, S., Lemoine, F. G., et al. (2012). Gravity field and internal structure of Mercury from MESSENGER. *Science*, *336*, 214–217.

Strangway, D. W., Sharpe, H., Gose, W., & Pearce, G. (1973). Lunar magnetic anomalies and the Cayley Formation. *Nature*, *246*, 112–114.

Strom, R. G., Chapman, C., Merline, W., Solomon, S., & Head III, J. W. (2008). Mercury cratering record viewed from MESSENGER's first flyby. *Science*, *321*, 79–81.

Thomas, R. J., Rothery, D. A., Conway, S., & Anand, M. (2014). Mechanisms of explosive volcanism on Mercury: Implications from its global distribution and morphology. *Journal of Geophysical Research: Planets*, *119*, 2239–2254. https://doi.org/10.1002/2014JE004692

Tsunakawa, H., Takahashi, F., Shimizu, H., Shibuya, H., & Matsushima, M. (2014). Regional mapping of the lunar magnetic anomalies at the surface: Method and its application to strong and weak magnetic anomaly regions. *Icarus*, *228*, 35–53.

Tsunakawa, H., Takahashi, F., Shimizu, H., Shibuya, H., & Matsushima, M. (2015). Surface vector mapping of magnetic anomalies over the Moon using Kaguya and Lunar Prospetor observations. *Journal of Geophysical Research: Planets*, *120*, 1160–1185. https://doi.org/10.1002/2014JE004785

Vasavada, A. R., Paige, D., & Wood, S. (1999). Near-surface temperatures on Mercury and the Moon and the stability of polar ice deposits. *Icarus*, *141*, 179–193.

von Frese, R. R. B., Hinze, W. J., & Braile, L. W. (1981). Spherical earth gravity and magnetic anomaly analysis by equivalent point source inversion. *Earth Planet Science Letters*, *53*, 69–83.

Weider, S. Z., Nittler, L., Murchie, S., Peplowski, P., McCoy, T., Kerber, L., et al. (2016). Evidence from MESSENGER for sulfur- and carbon-driven explosive volcanism on Mercury. *Geophysical Research Letters*, *43*, 3653–3661. https://doi.org/10.1002/2016GL068325

Weider, S. Z., Nittler, L. R., Starr, R. D., Crapster-Pregont, E. J., Peplowski, P. N., Denevi, B. W., et al. (2015). Evidence for geochemical terranes on Mercury: Global mapping of major elements with MESSENGER's X-Ray Spectrometer. *Earth Planet Science Letters*, *416*, 109–120.

Weider, S. Z., Nittler, L. R., Starr, R. B. D., McCoy, T. J., & Solomon, S. C. (2014). Variations in the abundance of iron on Mercury's surface from MESSENGER X-Ray Spectrometer observations. *Icarus*, *235*, 170–186.

Weiss, B. P., & Tikoo, S. (2014). The lunar dynamo. *Science*, *346*, 1198–1209.

Wieczorek, M. A., Weiss, B. P., & Stewart, S. T. (2012). An impactor origin for lunar magnetic anomalies. *Science*, *335*, 1212–1215.

Wright, J., Rothery, D. A., Balme, M. R., & Conway, S. J. (2016). Preliminary observations of Rustaveli basin, Mercury. Lunar Planet. Sci. XLVII, Abstract 2063.

Wright, J., Rothery, D. A., Balme, M. R., & Conway, S. J. (2018a). Geological mapping of the Hokusai (H05) quadrangle of Mercury: Status update. Lunar Planet. Sci. XLIX, Abstract 2064.

Wright, J., Rothery, D. A., Balme, M. R., & Conway, S. J. (2018b). Spatial distribution and morphometric measurements of circum-Caloris knobs on Mercury. Lunar Planet. Sci. XLIX, Abstract 2133.

Zuber, M. T., Smith, D., Phillips, R., Solomon, S., Neumann, G., Hauck II, S., et al. (2012). Topography of the northern hemisphere of Mercury from MESSENGER laser altimetry. *Science*, *336*, 217–220.